Supplementary Information

Water-mediated Recycling of Gold, Palladium, and Platinum Using Semimetallic TiS_2 and TaS_2 Nanosheets

Jianhong Wei[1]#, Miaofei Huang[1]#, Kuang Yu[1]*, Huanjing Liang[1], Fei Li[1], Kaiqiang Zheng[1], Fangluo Chen[1], Yibo Gao[1], Yang Su[1]*, Hui-Ming Cheng[2,3,4]*

[1]Institute of Materials Research, Shenzhen International Graduate School, Tsinghua University, Shenzhen, 518055, P. R. China
[2]Institute of Technology for Carbon Neutrality, Shenzhen Institute of Advanced Technology, Chinese Academy of Sciences, Shenzhen, 518055 P. R. China
[3]Faculty of Materials Science and Energy Engineering, Shenzhen University of Advanced Technology, Shenzhen, 518055 P. R. China
[4]Shenyang National Laboratory for Materials Science, Institute of Metal Research, Chinese Academy of Sciences, 72 Wenhua Road, Shenyang, 110016 P. R. China

These authors contributed equally: Jianhong Wei, Miaofei Huang;
*Corresponding authors:
yu.kuang@sz.tsinghua.edu.cn (K. Yu)
su.yang@sz.tsinghua.edu.cn (Y. Su);
hm.cheng@siat.ac.cn (H.-M. Cheng)

Supplementary Section 1 | Exfoliation of TiS_2 and TaS_2 nanosheets and their structure analysis

Transition metal dichalcogenides (TMDs) including TiS_2 and TaS_2 nanosheets were exfoliated following a previous study[1]. Briefly, the 1T-TiS_2 bulk flakes (0.2 g, Nanjing NXNANO Tech. Co., Ltd.) were mixed with 4 ml of 2 M LiOH aqueous solution and stirred for 1 hour under nitrogen. The intercalated 1T-TiS_2 powder was washed several times with deionized water until the pH was ~7. It was then onicated for 30 min in an ice bath to obtain a dispersion of 1T-TiS_2 nanosheets. The dispersion was centrifuged at 3000 rpm for 10 min and the supernatant was collected and used for extraction test. We used an identical procedure for the exfoliation of the 2H-TaS_2 nanosheets.

After exfoliation, the TMD nanosheets were analyzed using Raman, transmission electron microscope (TEM), atomic force microscope (AFM), and X-ray diffraction (XRD). For the Raman analysis (Fig. S1), similar to its bulk materials, the characteristic Raman peaks corresponding to A_{1g} (333 cm^{-1}) and E_g (227.2 cm^{-1}) vibration modes of 1T-TiS_2[2, 3], and peaks at the 204 cm^{-1}, 279 cm^{-1}, and 394 cm^{-1} due to the E_{1g}, E^1_{2g}, and A_{1g} lattice vibration modes of 2H-TaS_2 were evident[4]. There was no peak for other crystalline phases, suggesting the predominant phases of TiS_2 and TaS_2 were 1T and 2H respectively.

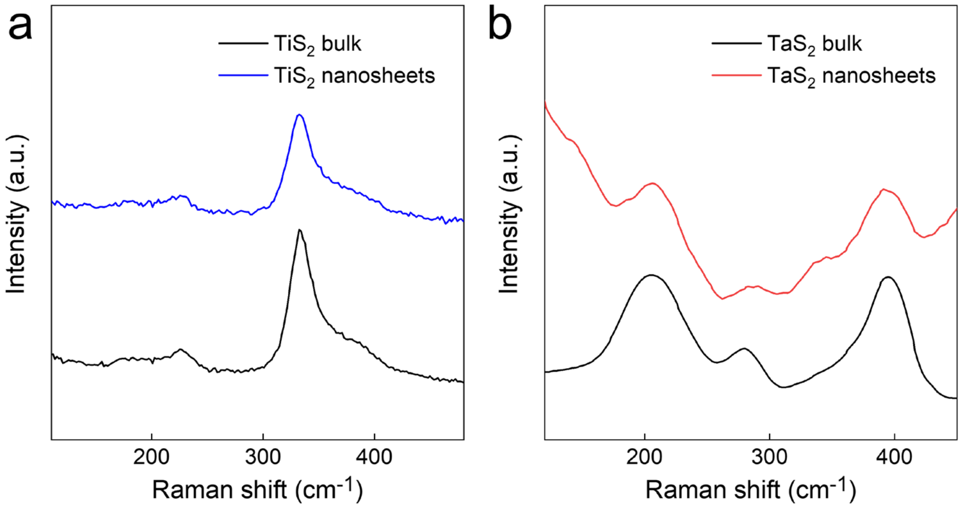

Figure S1. Raman spectra of bulk and exfoliated (a)TiS_2 and (b)TaS_2 nanosheets

Fig. S2 showed TEM images of representative exfoliated 1T-TiS_2 and 2H-TaS_2 nanosheets were 2D features with wrinkles, indicating successful exfoliation. The high-resolution TEM images clearly showed that the TiS_2 nanosheet had a lattice spacing of 0.267 nm, corresponding to its (101) crystal plane[5, 6], and the TaS_2 nanosheet had a lattice spacing of 0.290 nm, corresponding to its (100) crystal plane, the high-resolution TEM images showed high crystalline structure[7, 8], and the selected area electron diffraction (SAED) patterns of 1T-TiS_2 and 2H-TaS_2 showed no impurities, suggesting the good crystalline structure of the nanosheets.

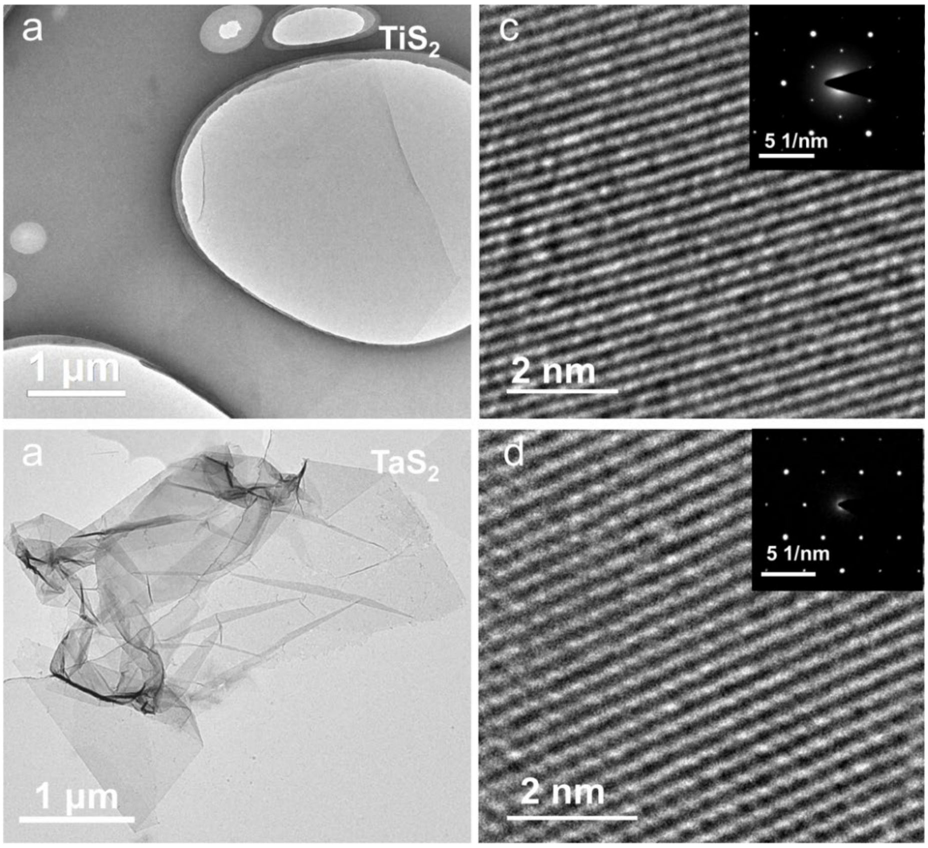

Figure S2. TEM analysis of exfoliated TMD nanosheets. Low-magnitude images of (a) TiS_2 and (b) TaS_2 nanosheet. High-resolution TEM images of (c) TiS_2 and (d) TaS_2 nanosheets and insets were their corresponding SAED patterns.

AFM analysis (Fig. S3) showed that the exfoliated nanosheets had a lateral size of 1-3 μm, and the thickness of both were in the range of 0.9 - 2.5 nm, indicating that they were mono- or few-layer.

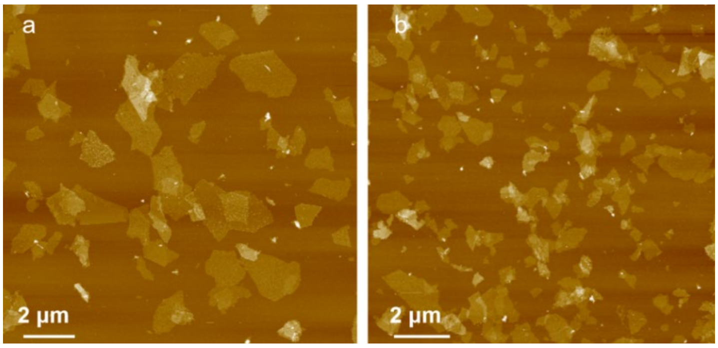

Figure S3. Thickness of the exfoliated nanosheets. (a) AFM image of exfoliated 1T-TiS_2 nanosheets. (b) AFM image of 2H-TaS_2 nanosheets.

For the XRD analysis, the patterns (Fig. S4) showed that the peaks of laminates assembled from the exfoliated TiS_2 (001) and TaS_2 (002) were slightly shifted to a lower angle compared to their corresponding powders, suggesting lattice expansion and successful exfoliation.

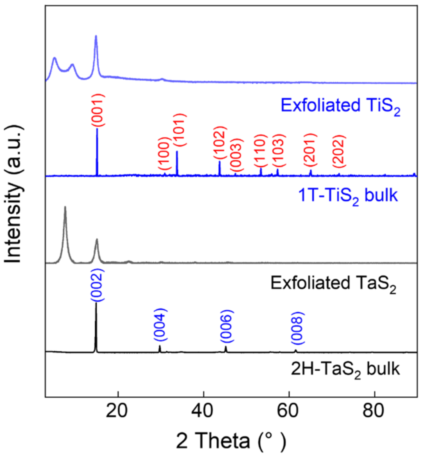

Figure S4. XRD patterns of laminates assembled from exfoliated (TiS_2 and TaS_2) nanosheets and their bulk powders.

Supplementary Section 2 | Precious metal (PM) extraction by TiS_2 and TaS_2 nanosheets

2.1 Economic analysis for PM extraction by TiS_2

The economic estimated value of recycled PM by per gram TiS_2 was calculated using Eq. (1).

$$Estimated\ \ value = Q_e \times PR \qquad \text{Eq. (1)}$$

where Q_e was the extraction capacity (g/g), and PR was the market price (RMB/g) of precious metals. The market prices for Au, Pd, and Pt in 2024 were approximately ￥420, ￥245, and ￥224 /g.

2.2 pH-dependent extraction capacities for different PM ions by TiS_2 nanosheets

The suitable pH values for PM extraction were determined from the Pourbaix diagram following a previous report and were illustrated in the main text[9, 10]. The extraction capacity (Q_e) for Au, Pt, and Pd ions at different pH values were measured and plotted versus the corresponding pH values (Fig. S5). It was worth noting that, despite Q_e changes with pH, it remained high, which was critical for a high and stable PM extraction.

For the extraction of $[AuCl_4]^-$, the Q_e remained stable the pH was in the range of 3-5. The decrease at pH<3 could be attributed to the protonation of TMD nanosheets, eliminating certain adsorption sites, hence giving a lower Q_e[11-13], while, the Q_e decrease at pH >5 was attributed to the hydrolysis of $[AuCl_4]^-$, forming a mixture of $[AuCl_4]^-$, $[AuCl_3(OH)]^-$, $[AuCl_2(OH)_2]^-$, $[AuCl_3(OH)_1]^-$ and $[Au(OH)_4]^-$ [11, 14], leading to a decrease in the reduction potenial[15, 16], hence a lower Q_e was observed. A similar phenomenon had been previously reported in the literature[11, 13, 16].

For extraction of $[PtCl_6]^{2-}$, the Q_e remained stable across the tested pH range 3-7, due to the stability of the Pt (IV) species within this range[9, 10]. The slight decrease in Q_e observed for both $[PtCl_6]^{2-}$ and $[PdCl_4]^{2-}$ at low pH could be attributed to the protonation of the nanosheets, similar to the case of $[AuCl_4]^-$.

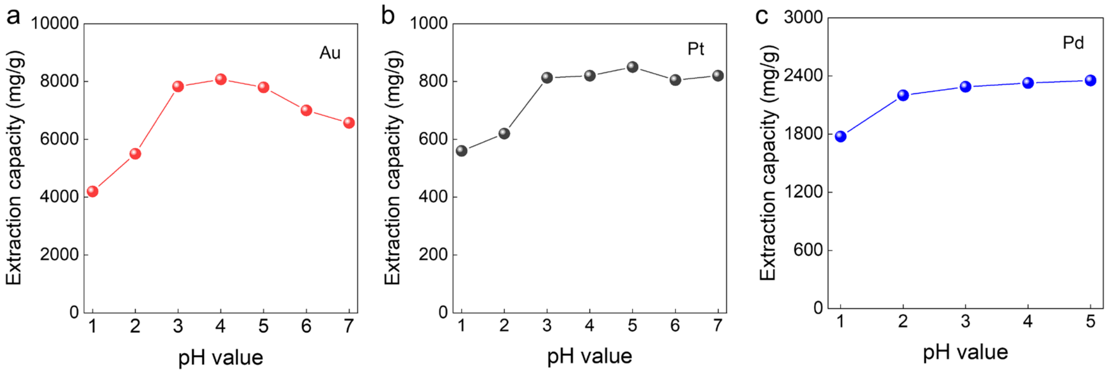

Figure S5. Extraction capacity of TiS_2 nanosheets at different pH values. Q_e values of TiS_2 nanosheets for (a) Au, (b) Pt, and (c) Pd ions at 10 ppm.

2.3 Removal efficiencies of different PM ions with different pH by TiS_2 nanosheets

To determine the PM removal efficiency of TiS_2 nanosheets, we used an initial PM concentration of 10 ppm, and the weight ratios between the Au, Pd, and Pt ions to TiS_2 were set at 3:1, 1:1, and 0.1:1, respectively. The mixture at different extraction time was sampled to study the removal kinetics. The removal efficiency (R) was calculated using Eq. (2).

$$R = \frac{(C_0 - C_e)}{C_0} \times 100\% \qquad \text{Eq. (2)}$$

where C_0 (mg/L) and C_e (mg/L) were the initial concentration and equilibrium concentrations, respectively, and were determined using inductively coupled plasma optical emission spectroscopy (ICP-OES).

The removal efficiencies at different pH values were also determined using a similar procedure with changing extraction pH using NaOH or HCl.

2.4 Comparison of Q_e achieved by TiS_2 and TaS_2 nanosheets with previous reports.

Table S1: Extraction capacities of various gold adsorbents.

Metal ion	**Adsorbent**	**C_0 (ppm)**	**Q_e (mg/g)**	**Ref.**
Au(III)	rGO	10	1850	17
Au(III)	MOF/PpPD	＞4000	1600	12
Au(III)	Polycarbene	5000	2090	18
Au(III)	H-bond COF	300	1725	19
Au(III)	Porous porphyrin	＞3000	1970	20
Au(III)	MOF/PpPDA	1000	934	21
Au(III)	Amidoxime-MOF	＞600	954	22
Au(III)	NH_2-CTFs	>25	909	23
Au(III)	N-MXene	1000	1198	24
Au(III)	Py-MoS_2	＞1700	3343	25
Au(III)	GO/CS sponge	>200 >2000	3573 7810	26
Au(III)	S-PAcH	>200	~2847	27
Au(III)	CNT/2H-MoS_2	1000	2495	28
Au(III)	TaS_2	10	4100	This Work
		1	3966	
	TiS_2	100	8073	
		10	8076	
		1	8084	
Pd(II)	CITCF	~500	~929	29
Pd(II)	POP-oNH_2-Py	~800	752	30
Pd(II)	MXene	~200	184.56	31
Pd(II)	COF-TzDa	~482	265.4	32
Pd(II)	MOF-NH_2	~1600	167	33
Pd(II)	PAN/MOF-NH_2	＞700	165.8	34
Pd(IV)	Py-MoS_2	~500	~1000	25
Pd(IV)	Py-SnS_2	>400	1103.72	10
Pd(II)	TaS_2	10	1100	This Work
		1	1009	
	TiS_2	100	2359	
		10	2217	
		1	1892	

Metal ion	**Adsorbent**	**C_0 (ppm)**	**Q_e (mg/g)**	**Ref.**
Pt(IV)	Py-SnS_2	＞400	617.61	10
Pt(IV)	DG-POP-2	＞50	388	35
Pt(IV)	Py-MoS_2	~500	~829	25
Pt(IV)	PAN/MOF-NH_2	＞700	172.5	34
Pt(II)	SCU-COF-3	＞200	168.4	36
Pt(IV)	Chitosan- l-lysine	~400	~129	37
Pt(II)	supramolecular polymers	1-2	33	38
Pt(IV)	S-PAcH	~200	~714	27
Pt(II)	BIT-POPs	＞250	~360	39
Pt(II)	COP-180	~1000	~197	20
Pt(IV)	TaS_2	10	452	This Work
		1	439	
	TiS_2	100	1154	
		10	813	
		1	323	

Supplementary Section 3 | Supplementary evidence for the PM extraction mechanism

3.1 Characterization of TiS_2@PM

After PM extraction, the PM-adsorbed TiS_2 nanosheets were collected and analyzed using TEM, XPS, and XRD.

TEM coupled with energy-dispersive X-ray spectroscopy (EDS) was used to study the distribution of chemical elements in TiS_2@PM (Fig. S6). All PM elements were evenly distributed on both the edges and the in-plane surfaces of the TiS_2 nanosheets.

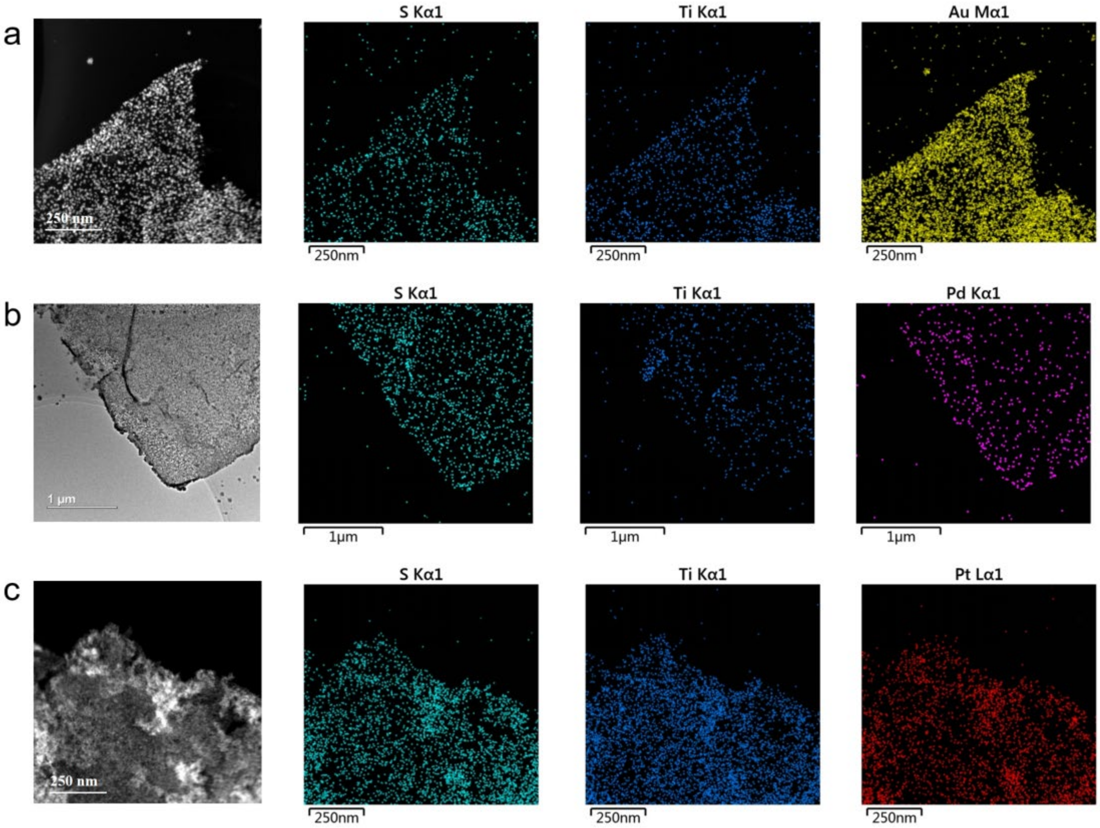

Figure S6. TEM-EDS elemental analysis of TiS_2 nanosheets after (a) Au, (b) Pd, and (c) Pt adsorption.

To supplement the TEM observation in Fig. 3, Fig. S7 showed the high-resolution TEM images and the corresponding SAED patterns of TiS_2@PM, confirming the simultaneous deposition of Au^0, Pd^0, and PtS nanoparticles.

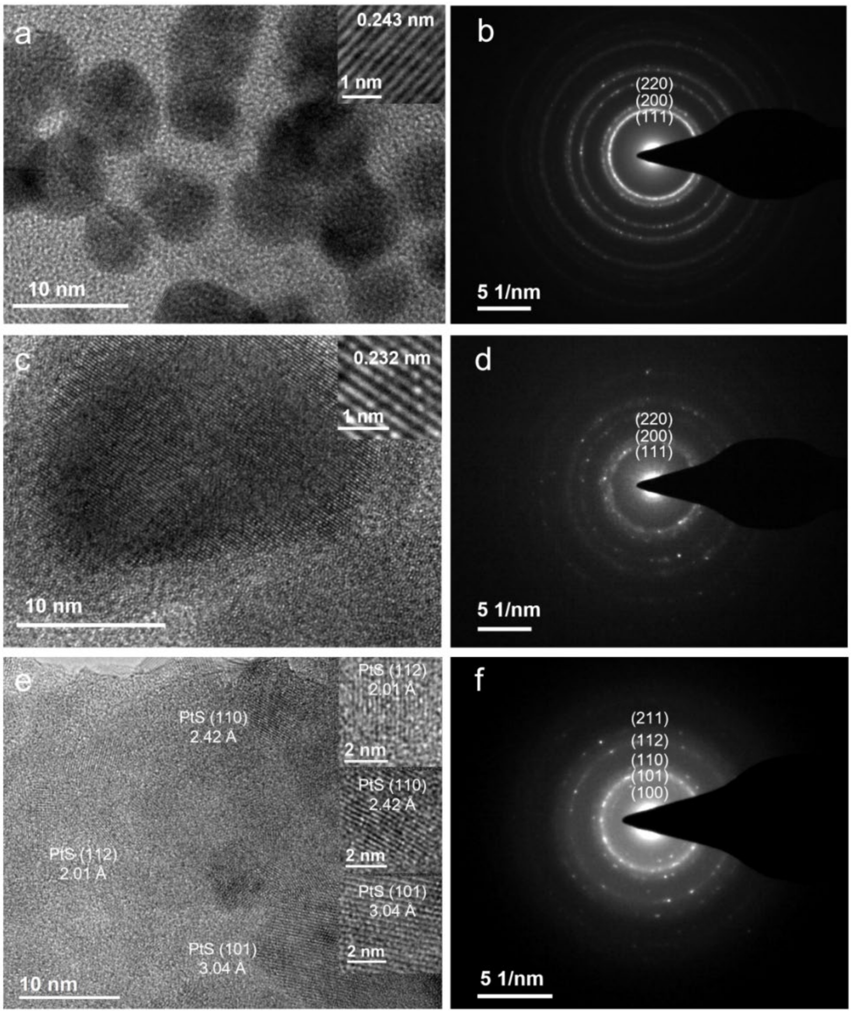

Figure S7. Simultaneous deposition of PM-containing nanoparticles. (a) High-resolution image of TiS_2@$[AuCl_4]^-$ and (b) corresponding SAED pattern. (c) High-resolution image and (d) corresponding SAED pattern acquired from TiS_2@$[PdCl_4]^{2-}$. (e) High-resolution image and (f) corresponding SAED pattern acquired from TiS_2@$[PtCl_6]^{2-}$. The corresponding crystalline orientations of Au, Pd, and PtS were labeled in (b), (d), and (f) respectively.

We also used X-ray photoelectron spectroscopy (XPS) to examine the chemical composition of TiS_2@PM precipitates. The wide-range XPS spectra of TiS_2 after absorption showed the existence of O1s, Ti2p, S2p, Pd3d, Pt4f, and Au4f peaks (Fig. S8). Notably, XPS of TiS_2@$[AuCl_4]^-$ showed a weak sulfur peak which was consistent with S^{2-} being oxidized to soluble sulfate species.

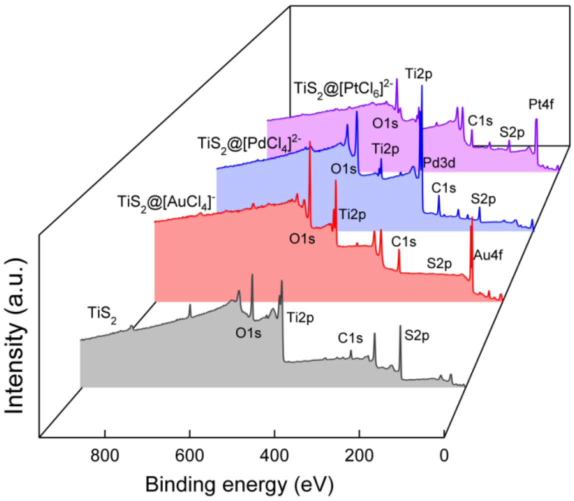

Figure S8. Wide-range XPS spectra of TiS_2 nanosheets and TiS_2@PM after 24 hours of adsorption.

Not only $[AuCl_4]^-$, $[PdCl_4]^{2-}$, and $[PtCl_6]^{2-}$, TiS_2 nanosheets were efficient for other Au-, Pd-, Pt- and Ag-containing ions with a reduction potential higher than +0.59 V, in addition, to supplement the Q_e shown in Fig. 3 of the main text, we had provided further XRD spectra of TiS_2 after its extraction of $[AuBr_4]^-$, $Ag^+(AgNO_3)$, $[AuI_4]^-$, $[RhCl_6]^{3-}$ and $[Au(S_2O_3)_2]^{3-}$. As shown in Fig. S9, the diffraction peaks assigned to metallic Au, and Ag appeared in the XRD patterns of $TiS_2@[AuBr_4]^-$, $TiS_2@[AuI_4]^-$, and $TiS_2@Ag^+$, suggesting a reductive extraction, consistent with the observed high Q_e shown in Fig. 3, but the diffraction peaks for metallic gold were absent for $[Au(S_2O_3)_2]^{3-}$ for which TiS_2 had a negligible Q_e, similar to $[RhCl_6]^{3-}$.

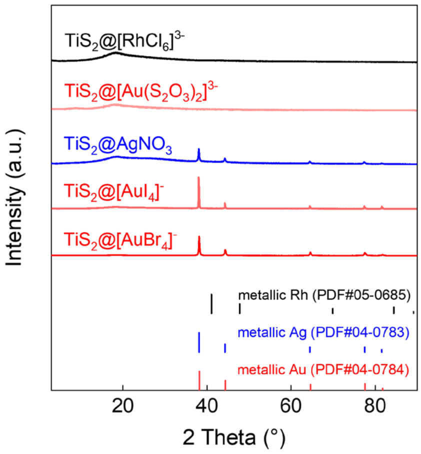

Figure S9. XRD patterns of $TiS_2@[AuBr_4]^-$, $TiS_2@[AuI_4]^-$, $TiS_2@$ $[Au(S_2O_3)_2]^{3-}$, $TaS_2@AgNO_3$, and $TiS_2@$ $[RhCl_6]^{3-}$. The diffraction peak positions of metallic Rh, Ag, and Au from the standard PDF card were indicated at the bottom.

3.2 Work functions of TiS_2 and TiS_2 nanosheets

The work function (Φ) of semimetallic TiS_2 and TaS_2 nanosheets was a direct indicator of their reduction potential, we, therefore, used ultraviolet photoelectron spectroscopy (UPS) to measure their Φ.

Φ was the minimum energy required to move an electron from inside a solid to its surface, and was defined as the difference between the vacuum level (E_{vac}) and the Fermi level (E_F), which could be expressed as follows:

$$\Phi = E_{vac} - E_F \qquad \text{Eq. (3)}$$

where E_F was defined as the highest energy level occupied by electrons at T = 0 K. and E_{vac} was the energy at which an electron was completely free and not influenced by the nucleus and was generally 0 eV.

Furthermore, because the difference between the vacuum level and the standard hydrogen electrode potential was 4.44 eV, the relationship between Φ and the reduction potential (versus Standard Hydrogen Electrode (vs SHE)) of a given material/ion was written as[40]:

$$E\ (\mathit{vs.}\mathrm{SHE}) = \Phi/e - 4.44\ \mathrm{V} \qquad \text{Eq. (4)}$$

Using Eq. (4), the work functions of TiS_2 and TaS_2 nanosheets can be translated into their reduction potentials, explaining their reductive adsorption to the PM ions.

Fig. S10 showed the UPS spectra of TiS_2 and TaS_2 that we used to determine Φ. According to Eq. (5),

$$\Phi = h\nu - (E_{cutoff} - E_F) \qquad \text{Eq. (5)}$$

where E_{cutoff} was the inelastic secondary electron cutoff, E_F was the Fermi level edge[41], and the photon energy (hν) of the excitation light used for our measurement was 21.22 eV. E_{cutoff} values of TiS_2 and TaS_2 were respectively determined to be 17.27 and 17.33 eV, and the E_F of TiS_2 and TaS_2 was ~0, yielding the work functions for TiS_2 and TaS_2 of 3.89 eV and 3.95 eV, respectively. Using Eq. (4), the reduction potentials of TiS_2 and TaS_2 were respectively -0.55 V and -0.49 V (vs. SHE)[40, 42, 43].

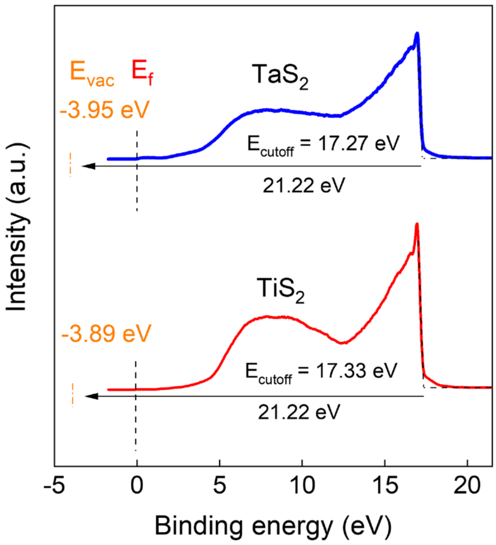

Figure S10. UPS spectra for work function measurements.

To supplement Fig. 3f and g, Fig. S11 showed the reduction potential of the ions used in this study versus the calculated equivalent reduction potential of TiS_2 and TaS_2, which clearly showed that an energy difference of ~1 eV was required for the reductive extraction by TiS_2 and TaS_2[42, 43], and such a difference could be due to the energy required for ion diffusion, ion desolvation, and the crystal nucleation and growth of Au, Pd, and PtS.

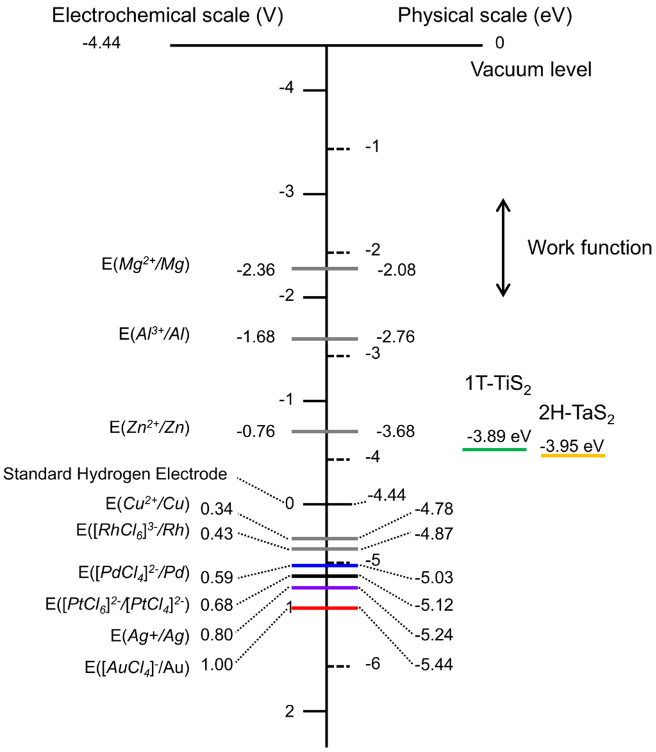

Figure S11. Comparison of reduction potentials of the ions studied and the work functions of TiS_2 and TaS_2 nanosheets.

3.3 Gold extraction capacities of the unexfoliated TMD and exfoliated ones

To study the influence of surface area on Q_e, we measured the Q_e (C_0 =100 ppm) for $[AuCl_4]^-$ of unexfoliated TMDs using an identical procedure used for the exfoliated ones. As shown in Fig. S12, the Q_e values of unexfoliated TiS_2 and TaS_2 were <1000 mg/g, significantly lower than for the exfoliated nanosheets, suggesting the large surface area of the exfoliated ones provides more PM adsorption sites, giving a high Q_e.

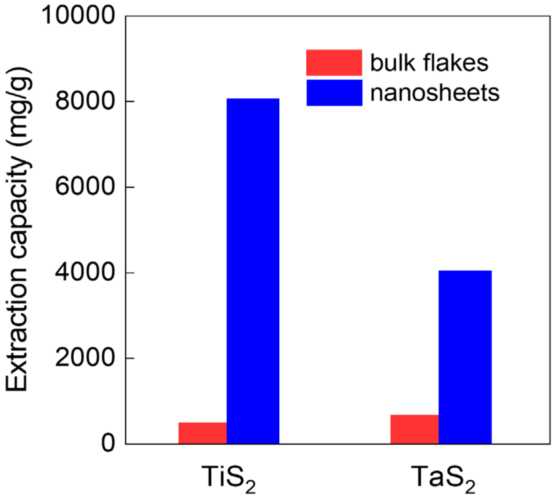

Figure S12. Extraction capacity of TiS_2 and TaS_2 nanosheets compared with flakes.

3.4 XPS analysis of TMD and the byproduct salt after PM extraction

Fig. S13 compared the XPS peaks of Ti and S before and after gold extraction. Compared with the pristine TiS_2, both Ti2p and S2p peaks shifted to a higher binding energy, suggesting the proposed electron donation. The deconvoluted Ti2p peaks showed that the Ti-S bond had changed to the Ti-O bond after gold extraction.

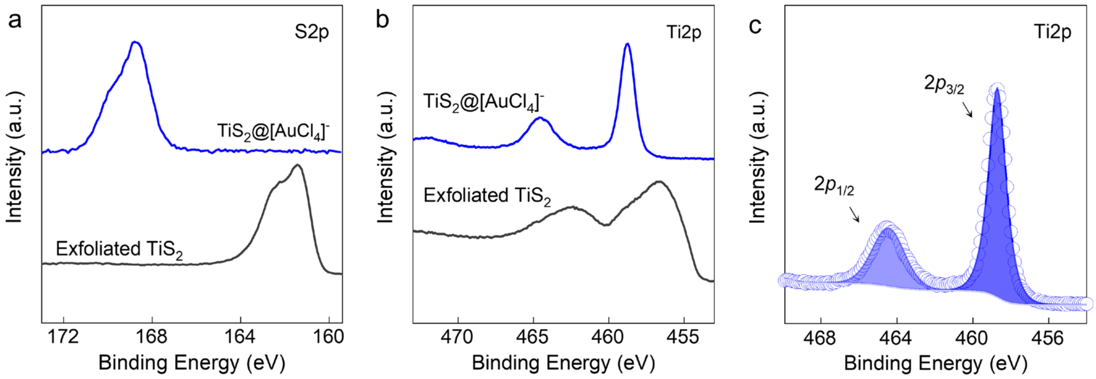

Figure S13. XPS peaks of Ti and S before and after gold extraction. (a) XPS S2p spectra of dissolved salt collected after PM adsorption compared with pristine TiS_2. (b) XPS Ti2p spectra of $TiS_2@[AuCl_4]^-$ precipitates compared with pristine TiS_2. (c) Deconvoluted XPS Ti2p spectra of $TiS_2@[AuCl_4]^-$ precipitates.

Not only the sulfur of TiS_2 (Fig. 4a) but also that of TaS_2 was the primary electron donation site. As shown in Fig. S14, we first analyzed the sulfur dissolved during the gold extraction by TaS_2, the peaks at 168.6 eV and 169.8 eV were assigned to sulfate species, similar to Fig. 4a. Furthermore, Ta4f of TaS_2 after gold extraction showed two peaks at 26.6 and 28.5 eV, both assigned to Ta^{5+} (Fig. S14b)[44, 45], suggesting that Ta^{4+} was oxidized to Ta^{5+} during the reductive extraction.

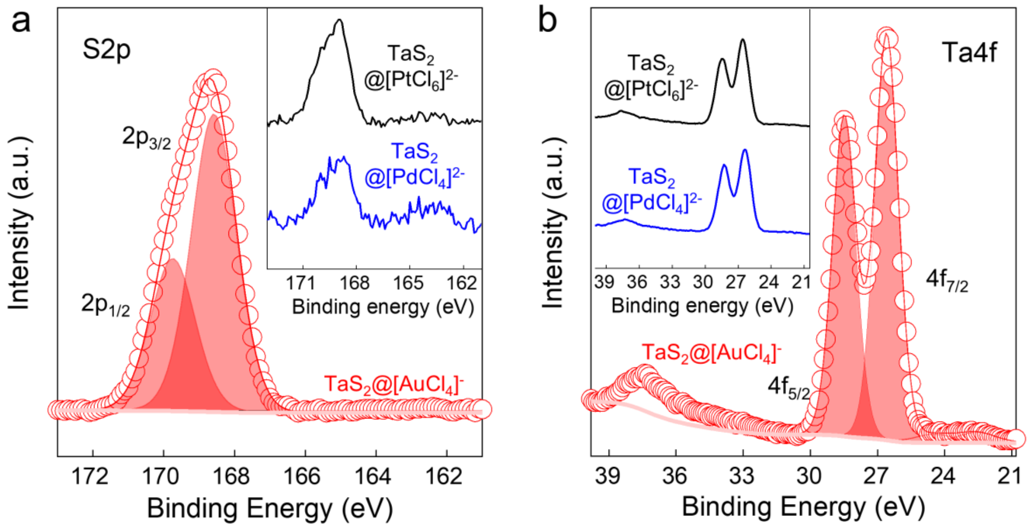

Figure S14. XPS analysis for the transformation of sulfur for TaS_2 after PM adsorption. (a) Deconvoluted S2p peaks of dissolved compounds collected after PM adsorption by TaS_2. The red line represents $TaS_2@[AuCl_4]^-$. Inset were the XPS S2p spectra of $TaS_2@[PdCl_4]^{2-}$ (blue line) and $TaS_2@[PtCl_6]^{2-}$ (black line). (b) Deconvoluted Ta4f peaks for the TaS_2@PM precipitate after adsorption. The red line represents $TaS_2@[AuCl_4]^-$. Inset were the XPS S2p spectra of $TaS_2@[PdCl_4]^{2-}$ (blue) and $TaS_2@[PtCl_6]^{2-}$ (black).

3.5 Calculation of the electron donation number during reductive extraction

The number of donated electrons from each TiS_2 molecule to $[AuCl_4]^-$ was calculated using Eq. (6).

$$N_e = \frac{Mr_{TiS_2} \times Q_e}{Mr_{Au}} \times n \qquad \text{Eq. (6)}$$

where N_e was electron donation numbers per TMD molecule. M_{TiS_2} and M_{Au} were the molar masses of TiS_2 (~112 g/mol) and Au (~197 g/mol), respectively. Q_e was the extraction capacity of TiS_2 for $[AuCl_4]^-$. n was 3 as three electrons were required for the reduction of $[AuCl_4]^-$ to Au^0. For a Q_e of 8073 mg/g for $[AuCl_4]^-$, this suggested that each TiS_2 molecule donated >13 electrons during the adsorption process.

3.6 The role of water in the gold extraction process by TiS_2 nanosheets

The critical role of water was probed by monitoring the pH change during gold extraction, as the water dissociation released H^+, decreasing the pH. Indeed, as shown in Fig.S15, the pH decreased from 3.96 to 3.77 during the 24-hour adsorption process, confirming the dissociation of water.

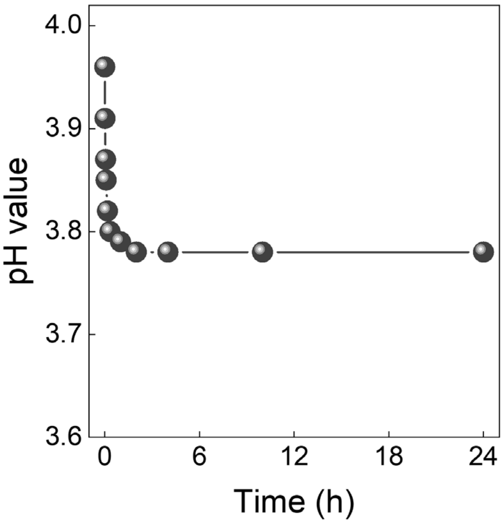

Figure S15. pH value of the $KAuCl_4$ aqueous solution (C_0 =10 ppm) after adding TiS_2 nanosheets.

Next, the solvent used for gold extraction was replaced by acetone. To determine the $[AuCl_4]^-$ concentration in acetone, we measured the UV-Vis spectra of a series of acetone solutions with $[AuCl_4]^-$ concentrations from 0 ppm to 100 ppm, and found a good linearity (R^2=0.999) between concentration and adsorption at 340 nm (Fig. S16a). We, therefore, used a C_0 of 100 ppm to study the influence of the organic solvent on Q_e, and found its Q_e decreased to 1180 mg/g. Adding water to the acetone (water volume ratio of 30%), again, we used UV-Vis spectra to determine the ion concentration and found linearity between the concentration and the adsorption intensity (ABS) at 340 nm (Fig. S16b), with this linear relationship (R^2=0.999), we determined that Q_e after adding 30 vol% water to the acetone increased to 5217 mg/g.

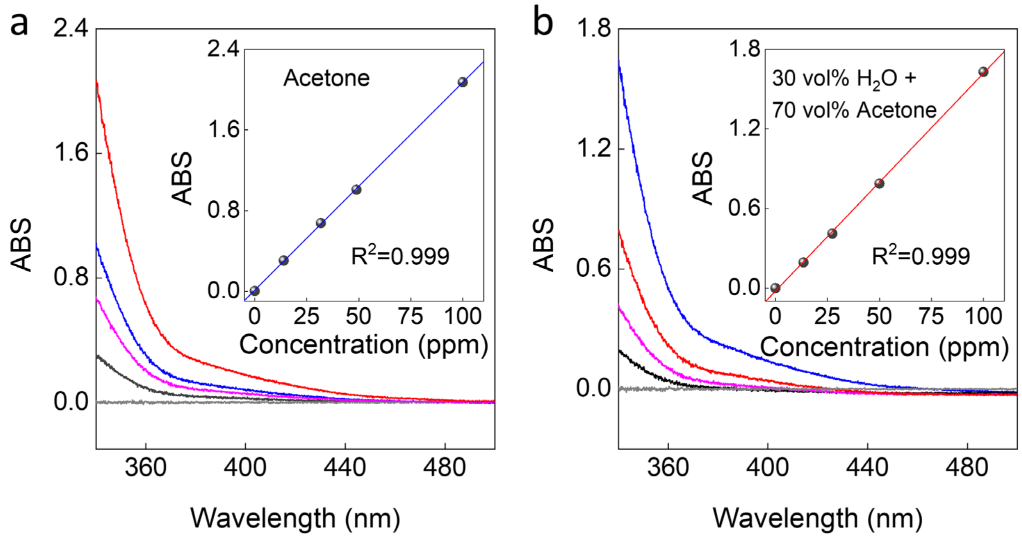

Figure S16. Evolution of the UV−vis spectra for different solutions with different $KAuCl_4$ concentrations. UV−vis spectra of (a) acetone and (b) 30 vol%-water-70 vol%-acetone solution of $KAuCl_4$. Insets were linear relationships between the absorbance at λ = 340 and the corresponding $KAuCl_4$ concentration.

3.7 DFT calculations

To understand the role of water in the extraction process, spin-polarized density functional theory (DFT) calculations were conducted as implemented in the Vienna Ab Initio Simulation Package (VASP). The interactions between ions and electrons were described using projector-augmented wave (PAW) pseudo-potentials. The exchange-correlation effects were treated with the Perdew-Burke-Ernzerhof (PBE) functional within the framework of the generalized gradient approximation (GGA).

A monolayer slab model of 1T-TiS_2 was constructed to represent the dechlorination reduction process of $[AuCl_4]^-$ by TiS_2 in an aqueous solution. For the structural optimization of 1T-TiS_2 crystal cells, a plane-wave energy cutoff of 600 eV was used, along with Gaussian smearing of 0.05 eV. A gamma-centered Monkhorst-Pack of 9×9×5 k-point grids was used for 1T-TiS_2. To simulate the two-dimensional interface, periodic structures of 8×8×1 supercells of 1T-TiS_2 were constructed with a vacuum thickness of 15 Å.

For the calculations, a reduced plane-wave energy cutoff of 450 eV was used, along with Gaussian smearing and a 2×2×1 gamma-centered Monkhorst-Pack k-point grid. Electronic self-consistency was achieved with an energy convergence criterion of 10^{-5} eV, and structural relaxations were performed until the forces on all atoms were below

0.02 eV/Å for all calculations. In addition, the implicit solvent model was used to compute the energy diagram of the dechlorination reduction process of $[AuCl_4]^-$ and 1T-TiS_2 in aqueous solution.

Supplementary Section 4 | PM Recovery from real-world waste streams

For Au recovery from electronic waste(e-waste), five pieces of scrap computer central processing unit (CPU) boards were digested using 20 mL aqua regia at 60 °C for 12 hours. Subsequently, the solid waste was removed by filtering the digested mixture through a 0.22 μm pore size polyethersulfone (PES) membrane. The pH of the filtered leachate was then adjusted using 0.5 M NaOH to give a pH of ~2, resulting in an Au ion concentration of ~16.3 ppm. Subsequently, TiS_2 nanosheets (~3 mg) were added to the 100 mL leachate with stirring for 24 hours. Finally, the resulting mixture was filtered through a 0.22 μm membrane to obtain Au-adsorbed TiS_2 and the filtrate. The removal efficiency of the filtrate was determined by ICP-OES using Eq. (2) in supplementary section 2. Finally, the obtained Au-adsorbed TiS_2 was washed with deionized water and dissolved in 5 mL of aqua regia, yielding a concentrated Au solution and insoluble Ti-containing precipitates. We used scanning electron microscopy (SEM, Hitachi SU8010) -EDS to quantify the element composition of these precipitates and found that Ti (61 wt%), O (33 wt%), and other elements (~6 wt%, such as C) were present in the sample (Fig. S17b). The Au ions were reduced with $NaBH_4$ to obtain a metallic gold nugget. EDS analysis confirmed that the sample contained over 97 wt% Au (Fig. S17a), with ~3 wt% of carbon and oxygen elements possibly from the environment.

For Pt recovery from scrap catalysts, the 0.2 g fuel cell catalyst (Pt/C, obtained from Sinerosz) was first digested using 20 mL aqua regia with stirring at 60°C for 12 hours and then filtered to obtain a Pt-containing leachate. The pH of the leachate was adjusted with 0.5 M NaOH to give a pH of ~3, yielding a Pt concentration of 39.6 ppm. Next, 15 mg of TiS_2 was added into a 50 mL leachate with stirring for 24 hours. Subsequently, the resulting mixture was filtered to obtain Pt-adsorbed TiS_2 and filtrate. The removal efficiency of the filtrate was determined by ICP-OES. Finally, we used the same reduction method for Au recycled from the e-wastes, to separate Pt from TiS_2. EDS analysis (Fig. S17c) showed that the purity of Pt exceeds 97 wt%, with ~3 wt% of C and O present.

For Pd recovery from scrap catalysts, 0.1 g Pd/C catalyst (purchased from Alibaba) was soaked into 10 mL aqua regia for 12 hours stirring at 60°C and then filtered to obtain a leachate. The pH of the leachate was adjusted with 0.5 M NaOH to give a pH of ~2, yielding a Pd concentration of ~ 43 ppm. 5 mg of TiS_2 was then added to 50 mL of leachate with stirring for 24 hours and further filtered to obtain Pd-adsorbed TiS_2 and filtrate, resulting in a Pd concentration reduced to 0.141 ppm and 99% recovery of the Pd. Finally, we used the same reduction method for Au recycled from the e-wastes to separate the Pd from TiS_2. EDS analysis (Fig. S17d) showed the purity of Pd was > 97 wt%, with ~3 wt% of C and O elements.

For the recycling of platinum and palladium from spent automotive catalytic converters (ACCs), we followed previous reports[46, 47], The spent ACCs (120 g, purchased from Alibaba) were firstly pulverized and soaked in 500 mL of a 1 M NaOH aqueous solution for 24 h to remove Al_2O_3. The solid powder was collected by filtration and then digested using 40 mL aqua regia diluted with 200 mL deionized water. The mixture was then heated (1500 W, 1 hour) at 180 °C using a microwave digester instrument (Honeycomb XH-800X) to dissolve the PM, after which the mixture was filtered, and the filtrate was the leachate of PM ions (pH ~2). Subsequently, following the process flow depicted in Fig. 5d, we added the first TiS_2 nanosheets (20 mg) to the 200 mL of the leachate to recycle the Pd ions for 10 minutes. The TiS_2 with adsorbed Pd was then separated from the leachate, and a second batch of TiS_2 nanosheets (20 mg) was added to the resultant leachate to extract Pt for 36 hours. The TiS_2 nanosheets with adsorbed Pt were separated from the leachate, leaving leachate without or with little Pd and Pt, but ~18 ppm of Rh ions. We added iron powder (100 mg) to this leachate and recycled Rh was obtained in the form of precipitates. For the separation of Pt and Pd from TiS_2, we followed the same reduction method for the Au recycled from the e-wastes. The purity of Pd after the first-step purification step was ~88 wt% (with ~11 wt% Pt), while the Pt purity after the second-step was ~98 wt% (Fig. S17e and Fig. S17f).

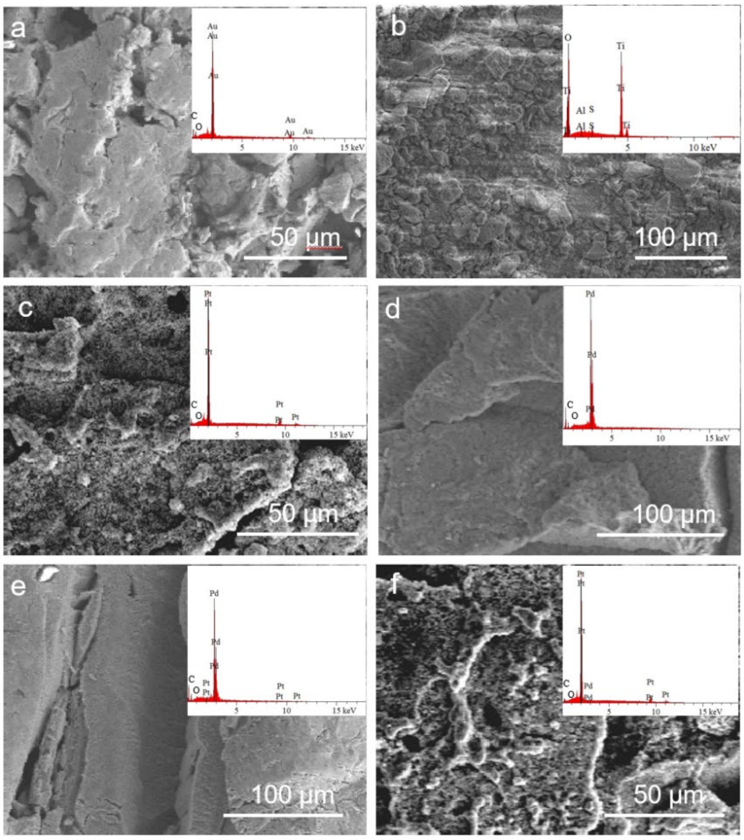

Figure S17. SEM-EDS analysis of PM nuggets and Ti-containing precipitates from their recycling process. SEM images of (a) Gold nugget and (b) Ti-containing precipitates from CPU recycling. SEM images of (c) Pt nugget and (d) Pd nugget from Pt/C and Pd/C recycling, respectively. SEM images of (e) Pd nugget and (f) Pt nugget from ACCs recycling. Insets were their corresponding EDS energy spectra.

References

1. Deng, F. et al. Regulating the Electrical and Mechanical Properties of TaS_2 Films via van der Waals and Electrostatic Interaction for High Performance Electromagnetic Interference Shielding. *Nano-Micro Letters* **15**, 106 (2023).
2. Li, Y. et al. Making Large-Area Titanium Disulfide Films at Reduced Temperature by Balancing the Kinetics of Sulfurization and Roughening. *Advanced Functional Materials* **30**, 2003617 (2020).
3. Yao, T. et al. Encapsulation of Titanium Disulfide into MOF-Derived N,S-Doped Carbon Nanotablets Toward Suppressed Shuttle Effect and Enhanced Sodium Storage Performance. *Small* **20**, 2311126 (2024).
4. Wang, S. et al. Organic covalent modification to improve thermoelectric properties of TaS_2. *Nature Communications* **13**, 4401 (2022).
5. Tang, J. et al. MXene derived TiS_2 nanosheets for high-rate and long-life sodium-ion capacitors. *Energy Storage Materials* **26**, 550-559 (2020).
6. Telkhozhayeva, M. et al. 2D TiS_2 flakes for tetracycline hydrochloride photodegradation under solar light. *Applied Catalysis B: Environmental* **318**, 121872 (2022).
7. Kovalska, E. et al. Photocatalytic activity of twist-angle stacked 2D TaS_2. *npj 2D Materials and Applications* **5**, 68 (2021).
8. Liu, W. et al. Experimental observations and density functional simulations on the structural transition behavior of a two-dimensional transition-metal dichalcogenide. *Scientific Reports* **10**, 18255 (2020).
9. Peng, Y. et al. Laser Assisted Solution Synthesis of High Performance Graphene Supported Electrocatalysts. *Advanced Functional Materials* **30**, 2001756 (2020).
10. Wang, R. et al. Interfacial Coordinational Bond Triggered Photoreduction Membrane for Continuous Light-Driven Precious Metals Recovery. *Nano Letters* **23**, 2219-2227 (2023).
11. Zhao, M., Huang, Z., Wang, S. & Zhang, L. Ultrahigh efficient and selective adsorption of Au(III) from water by novel Chitosan-coated MoS_2 biosorbents: Performance and mechanisms. *Chemical Engineering Journal* **401**, 126006 (2020).
12. Xue, T. et al. A customized MOF-polymer composite for rapid gold extraction from water matrices. *Science Advances* **9**, eadg4923. (2023).
13. Yu, C.-X. et al. Fabrication of Carboxylate-Functionalized 2D MOF Nanosheet with Caged Cavity for Efficient and Selective Extraction of Uranium from Aqueous Solution. *Small* **20**, 2308910 (2024).
14. Zhang, M. et al. Immobilization of ionic liquids onto chloromethylated polystyrene as a strategy for highly efficient and selective recovery of Au(III) from gold slag and PCBs. *Separation and Purification Technology* **337**, 126479 (2024).
15. Bakhromi, D., Safarmamadzoda, S.M., Fritskii, I.O. & Muborakkadamov, D.A. Complex Formation of $H[AuCl_4]$ with 2-Methylimidazole. *Russian Journal of Inorganic Chemistry* **66**, 820-826 (2021).
16. Mei, D. & Yan, B. A 2D Acridine-Based Covalent Organic Framework for Selective Detection and Efficient Extraction of Gold from Complex Aqueous-Based Matrices. *Angewandte Chemie International Edition* **63**, e202402205 (2024).

17. Li, F. et al. Highly efficient and selective extraction of gold by reduced graphene oxide. *Nature Communications* **13**, 4472 (2022).
18. Li, X. et al. Porous organic polycarbene nanotrap for efficient and selective gold stripping from electronic waste. *Nature Communications* **14**, 263 (2023).
19. Qiu, J. et al. Porous Covalent Organic Framework Based Hydrogen-Bond Nanotrap for the Precise Recognition and Separation of Gold. *Angewandte Chemie International Edition* **62**, e202300459 (2023).
20. Hong, Y. et al. Precious metal recovery from electronic waste by a porous porphyrin polymer. *Proceedings of the National Academy of Sciences* **117**, 16174-16180 (2020).
21. Sun, D.T., Gasilova, N., Yang, S., Oveisi, E. & Queen, W.L. Rapid, Selective Extraction of Trace Amounts of Gold from Complex Water Mixtures with a Metal–Organic Framework (MOF)/Polymer Composite. *Journal of the American Chemical Society* **140**, 16697-16703 (2018).
22. Luo, J. et al. Selective and rapid extraction of trace amount of gold from complex liquids with silver(I)-organic frameworks. *Nature Communications* **13**, 7771 (2022).
23. Kong, H.-Y., Tao, Y., Ding, X. & Han, B.-H. Efficient gold recovery from waste electronic and electric equipment by amino-modified covalent triazine frameworks. *Chemical Engineering Journal* **463**, 142393 (2023).
24. Jung, Y. et al. Nitrogen-Doped Titanium Carbide ($Ti_3C_2T_x$) MXene Nanosheet Stack For Long-Term Stability and Efficacy in Au and Ag Recovery. *Small* **19**, 2305247 (2023).
25. Wang, R. et al. Interfacial Coordination Bonding-Assisted Redox Mechanism-Driven Highly Selective Precious Metal Recovery on Covalent-Functionalized Ultrathin 1T-MoS_2. *ACS Applied Materials & Interfaces* **15**, 9331-9340 (2023).
26. Yang, K. et al. Graphene/chitosan nanoreactors for ultrafast and precise recovery and catalytic conversion of gold from electronic waste. *Proceedings of the National Academy of Sciences* **121**, e2414449121 (2024).
27. Shin, S.S. et al. Efficient recovery and recycling/upcycling of precious metals using hydrazide-functionalized star-shaped polymers. *Nature Communications* **15**, 3889 (2024).
28. Liu, F., You, S., Wang, Z. & Liu, Y. Redox-Active Nanohybrid Filter for Selective Recovery of Gold from Water. *ACS ES&T Engineering* **1**, 1342-1350 (2021).
29. Song, K.S. et al. Porous polyisothiocyanurates for selective palladium recovery and heterogeneous catalysis. *Chem* **8**, 2043-2059 (2022).
30. Aguila, B. et al. A Porous Organic Polymer Nanotrap for Efficient Extraction of Palladium. *Angewandte Chemie International Edition* **59**, 19618-19622 (2020).
31. Mu, W. et al. Removal of radioactive palladium based on novel 2D titanium carbides. *Chemical Engineering Journal* **358**, 283-290 (2019).
32. Bai, Y. et al. Precise recognition of palladium through interlaminar chelation in a covalent organic framework. *Chem* **8**, 1442-1459 (2022).
33. Lin, S. et al. Effective adsorption of Pd(II), Pt(IV) and Au(III) by Zr(IV)-based metal–organic frameworks from strongly acidic solutions. *Journal of Materials Chemistry A* **5**, 13557-13564 (2017).

34. Liu, Y. et al. Super-Stable, Highly Efficient, and Recyclable Fibrous Metal–Organic Framework Membranes for Precious Metal Recovery from Strong Acidic Solutions. *Small* **15**, 1805242 (2019).
35. Xiong, J. et al. Cost-effective and high-performance biguanide-incorporated ionic porous organic polymer for selective recovery of Pd(II) and Pt(IV) from metallurgical wastewater. *Chemical Engineering Journal* **488**, 150772 (2024).
36. He, L. et al. Synergy of first- and second-sphere interactions in a covalent organic framework boosts highly selective platinum uptake. *Science China Chemistry* **66**, 783-790 (2023).
37. Fujiwara, K., Ramesh, A., Maki, T., Hasegawa, H. & Ueda, K. Adsorption of platinum (IV), palladium (II) and gold (III) from aqueous solutions onto l-lysine modified crosslinked chitosan resin. *Journal of Hazardous Materials* **146**, 39-50 (2007).
38. Chen, Z., Chan, A.K.-W., Wong, V.C.-H. & Yam, V.W.-W. A Supramolecular Strategy toward an Efficient and Selective Capture of Platinum(II) Complexes. *Journal of the American Chemical Society* **141**, 11204-11211 (2019).
39. Shi, J. et al. Porous Polypyrrolidines for Highly Efficient Recovery of Precious Metals through Reductive Adsorption Mechanism. *Advanced Materials* **36**, 2405731 (2024).
40. Qi, H. et al. Graphdiyne Oxides as Excellent Substrate for Electroless Deposition of Pd Clusters with High Catalytic Activity. *Journal of the American Chemical Society* **137**, 5260-5263 (2015).
41. Shi, X. et al. Protruding Pt single-sites on hexagonal $ZnIn_2S_4$ to accelerate photocatalytic hydrogen evolution. *Nature Communications* **13**, 1287 (2022).
42. Trasatti, S. The absolute electrode potential: an explanatory note (Recommendations 1986). *Pure and Applied Chemistry* **58**, 955-966 (1986).
43. Lide, D.R. CRC Handbook of Chemistry and Physics, 87th Edition. (Taylor & Francis, 2006).
44. Wang, W. et al. Tantalum pentoxide (Ta_2O_5 and Ta_2O_{5-x})-based memristor for photonic in-memory computing application. *Nano Energy* **106**, 108072 (2023).
45. Shi, J. et al. Two-dimensional metallic tantalum disulfide as a hydrogen evolution catalyst. *Nature Communications* **8**, 958 (2017).
46. Suoranta, T., Zugazua, O., Niemelä, M. & Perämäki, P. Recovery of palladium, platinum, rhodium and ruthenium from catalyst materials using microwave-assisted leaching and cloud point extraction. *Hydrometallurgy* **154**, 56-62 (2015).
47. Spooren, J. & Abo Atia, T. Combined microwave assisted roasting and leaching to recover platinum group metals from spent automotive catalysts. *Minerals Engineering* **146**, 106153 (2020).